Physics of Fluids

Quasi three-dimensional deformable blade element and unsteady vortex lattice reduced-order modeling of fluid–structure interaction in flapping wings

Cite as: Phys. Fluids **34**, 121903 (2022); https://doi.org/10.1063/5.0129128
Submitted: 03 October 2022 • Accepted: 21 November 2022 • Accepted Manuscript Online: 21 November 2022 • Published Online: 07 December 2022

R. Schwab, J. Reade and M. Jankauski

Physics of Fluids ARTICLE scitation.org/journal/phf

Quasi three-dimensional deformable blade element and unsteady vortex lattice reduced-order modeling of fluid–structure interaction in flapping wings

Cite as: Phys. Fluids **34**, 121903 (2022); doi: 10.1063/5.0129128
Submitted: 3 October 2022 · Accepted: 21 November 2022 ·
Published Online: 7 December 2022

R. Schwab, J. Reade, and M. Jankauski[a)]

AFFILIATIONS

Department of Mechanical & Industrial Engineering, Montana State University, 220 Roberts Hall, Bozeman, Montana 59717, USA

[a)]Author to whom correspondence should be addressed: mark.jankauski@montana.edu

ABSTRACT

Flapping, flexible insect wings deform under inertial and fluid loading. Deformation influences aerodynamic force generation and sensorimotor control, and is thus important to insect flight mechanics. Conventional flapping wing fluid–structure interaction models provide detailed information about wing deformation and the surrounding flow structure, but are impractical in parameter studies due to their considerable computational demands. Here, we develop two quasi three-dimensional reduced-order models (ROMs) capable of describing the propulsive forces/moments and deformation profiles of flexible wings. The first is based on deformable blade element theory (DBET) and the second is based on the unsteady vortex lattice method (UVLM). Both rely on a modal-truncation based structural solver. We apply each model to estimate the aeromechanics of a thin, flapping flat plate with a rigid leading edge, and compare ROM findings to those produced by a coupled fluid dynamics/finite element computational solver. The ROMs predict wing deformation with good accuracy even for relatively large deformations of 25% of the chord length. Aerodynamic loading normal to the wing's rotation plane is well captured by the ROMs, though model errors are larger for in-plane loading. We then perform a parameter sweep to understand how wing flexibility and mass affect peak deflection, mean lift and average power. All models indicate that flexible wings produce less lift but require lower average power to flap. Importantly, these studies highlight the computational efficiency of the ROMs—compared to the convention modeling approach, the UVLM and DBET ROMs solve 4 and 6 orders of magnitude faster, respectively.

I. INTRODUCTION

Flying insects often serve as model organisms in the study of sensorimotor and neuromuscular control because they have relatively simple neural systems, yet are able to perform sophisticated tasks.[1] Insects may utilize halteres to sense angular velocities of their bodies,[2] campaniform sensilla to detect strains of their legs and exoskeleton,[3] and Johnston's organs to detect vibrations in the antennae to sense airflow.[4] Some insects utilize campaniform sensilla (strain-sensitive mechanoreceptors) distributed across their wings to encode deformations such that they can adjust their flapping kinematics for improved flight control.[5–7] Information regarding the insect body's angular velocity is also believed to be encoded in wing deformation,[8,9] hence making wing-based mechanoreception an essential sensory modality in insects that lack dedicated gyroscopic sensing organs. Wing flexibility and deformation are, therefore, critical to flight in many insect species.

In addition to sensory functions, deformation also influences wings' aerodynamic performance. Insect wings undergo large deformations due to both aerodynamic and inertial forces.[10–12] The surrounding fluid affects the wing deformation and vice versa, leading to a strong fluid–structure coupling. Wing flexibility may reduce the energetic requirements of flapping, since strain energy stored in the wing during elastic deformations may be recovered later in the wingbeat.[13] Wing flexibility also has a significant influence on thrust production through passive wing pitching and bending, which lowers drag forces and strengthens vortex production near the wing surface, thereby increasing lift forces.[14–16] Wing mass and the relative contribution of inertial and aerodynamic forces also play a role in efficiency. Lift-to-drag ratio is higher in cases where aerodynamic forces dominate deformation (e.g., low wing mass), likely due to smaller shed vortices and thus lower drag forces.[17] Additionally, flexibility may benefit

wing–wing interactions, such as during clap and fling type flapping, to enhance force generation. Studies show that wing deformation improves leading edge vortex (LEV) attachment and wake capture, where the wing interacts with shed vortices from the previous flap cycle to enhance force production.[18]

Owing to the experimental limitations in real insects, the characterization of structural and fluid phenomena surrounding flapping wings often relies on computational modeling.[11,19–26] Fluid modeling usually involves computational fluid dynamics (CFD) to solve the Navier–Stokes equations—a set of partial differential equations that describe the conservation of mass and conservation of momentum in fluid flows.[27] This fluid model is often used in conjunction with structural solvers such as finite element analysis (FEA) to evaluate bilateral fluid–structure interactions (FSIs).[11,19,22] Computational models have driven much of our current understanding of flapping wing mechanics, such as the development of LEVs[28] and the influence of venation patterns on spatially variable stiffness.[29] Additionally, computational models provide a platform to compare the performance of flexible wings to idealized rigid wings, where the latter are mathematically convenient but unrealistic in natural contexts.[11,30] While these computational models are an accepted instrument for studying flapping wing flight, they necessitate considerable computational resources, often requiring several days to reach converged solutions for each simulation. They are consequently challenged by studies that consider large parameter spaces, for example variable wing morphologies, flapping kinematics and material properties.

Because of the solution times required by higher-order flapping wing models, reduced-order models (ROMs) have emerged as useful frameworks to efficiently perform parametric and optimization studies. The two most common ROMs in flapping wing flight are based on quasi-static blade element theory (BET) and unsteady vortex lattice method (UVLM).[22,26,31–34] BET functions by discretizing a wing into airfoils that run along the wing's chord. The local aerodynamic forces and moments are determined via thin airfoil theory and are subsequently integrated over the wing surface to give the net forces and moments. BET is typically used to model rigid wings but has been extended to flexible wings in some contexts. For example, a BET-based formulation was used to model flexible wings experiencing single-degree-of-freedom rotation,[35] but because of the simplified kinematics, such a model cannot accommodate lifting flow. Wang *et al.* used BET to describe the aerodynamics of twistable wings subject to multiple-degree-of-freedom rotation,[36] though the structural model in this work is not amendable to the anisotropic or spatially variable material properties present in real insect wings.[37] Walker and Taylor developed a similar BET model for twistable wings, where the twist angle must be prescribed within this approach.[38]

UVLM estimates pressure over the wing surface by treating the wing and shed wake as an infinitely thin sheet of discrete vortices. These vortices cause a velocity gradient across the wing and thus a pressure differential. This method has the advantage of being significantly faster than high-fidelity CFD while still accounting for many unsteady phenomena.[22,39] Compared to BET, UVLM is more commonly used to describe the mechanics of two-dimensional (2D) or three-dimensional (3D) flexible wings,[22,26,33] but is more computationally expensive as well. One method to reduce the computational costs of UVLM (perhaps at the expense of accuracy) is to use a quasi three-dimensional approximation, similar to the one employed by BET. For a wing discretized spanwise into n segments, a quasi-3D approach reduces the number of required calculations by at least a factor of n. Vector calculations being reduced to two dimensions further enhance computational savings. However, to our knowledge, no such model has been developed for flapping wing flight.

Given the importance of wing flexibility in insect flight and the limitations of existing flapping wing fluid–structure interaction (FSI) models, the goal of the present work is to develop two quasi-3D ROMs of flapping, flexible wings and to benchmark the accuracy and computational times enabled by these models against a more conventional high-fidelity (HiFi hereafter) approach. Each ROM must be capable of estimating wing deformation and the bulk propulsive forces and moments of flapping. The first ROM is rooted in BET but accommodates wing deformation; we, therefore, refer to this model as deformable blade element theory (DBET hereafter). The second ROM is based on a quasi-3D UVLM approach (simply UVLM hereafter).

The remainder of the paper is organized as follows. First, we formulate the ROMs and describe the basis of the HiFi computational model. Then, we apply each model to predict the deformation and aerodynamics of a thin rectangular plate flapping in a quiescent environment. We assume the wing has a rigid leading edge, since the vibration modes measured in insect wings indicate that deformation is more pronounced at the trailing edge relative to the leading edge.[40,41] Though the ROMs may generalize to more complex wing structures (e.g., realistic planforms, vein structures), it is prudent to first benchmark their accuracy in a simplified context. We then compare propulsive forces and wing deformations estimated by each model, and perform a parametric study to quantify how wing stiffness and mass affect lift, peak deflection and average power requirements. Finally, we discuss the utility of these models within the field of insect flight and address some of the model limitations.

II. MATHEMATICAL MODELING

A. Flapping kinematics

First, we establish a wing-fixed system that rotates with the wing's rigid body motion (Fig. 1). The reference frame kinematics are identical across all modeling efforts and originated in Ref. 42. A wing is situated in an $X-Y-Z$ inertial coordinate system. The $X-Y-Z$ coordinate system undergoes a finite rotation α about the positive X direction, where α denotes the roll angle (also called flap angle) of the wing. The resulting $x''-y''-z''$ coordinate system is then rotated about y'' by angle β, where β represents wing pitch (also called wing rotation). The ensuing $x'-y'-z'$ system experiences finite rotation γ about the z' axis, where γ is wing yaw (sometimes stroke deviation). The terminal wing-fixed $x-y-z$ coordinate system is bound to the wing's rigid body rotation, where the wing is rotating about fixed point O. The unit vectors in the wing fixed frame are $\mathbf{e}_x$, $\mathbf{e}_y$, $\mathbf{e}_z$ and are directed along the x, y, and z axes, respectively. The angular velocity $\boldsymbol{\Omega}$ is

$$\boldsymbol{\Omega} = \underbrace{(\dot{\alpha}\cos\beta\cos\gamma + \dot{\beta}\sin\gamma)}_{\Omega_x}\mathbf{e}_x + \underbrace{(\dot{\beta}\cos\gamma - \dot{\alpha}\cos\beta\sin\gamma)}_{\Omega_y}\mathbf{e}_y + \underbrace{(\dot{\gamma} + \dot{\alpha}\sin\beta)}_{\Omega_z}\mathbf{e}_z, \tag{1}$$

where Ω_x, Ω_y, and Ω_z are the x, y, and z components of angular velocity with respect to the wing-fixed coordinate system.

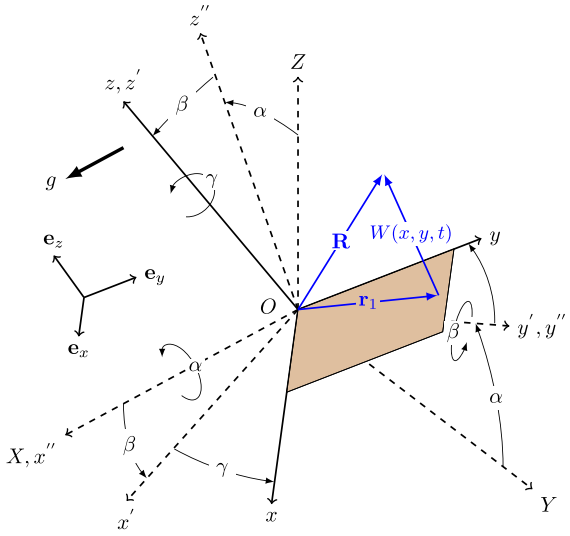

FIG. 1. Development of a $x-y-z$ coordinate system that rotates with the wing's rigid body motion. **R** is a position vector between the wing's fixed point of rotation O and a differential mass dm. Per our coordinate convention, gravity g acts in the $-X$ direction.

B. Reduced-order modeling

1. Structural modeling

Next, we derive a reduced-order structural modeling of the rotating, flexible wing. The structural model is general in the sense that it can incorporate any planar wing geometry and can interface with any appropriate fluid dynamic model. Within this work, we use this structural model in conjunction with the DBET and UVLM aerodynamic solvers. The benefit to this approach is that we must solve only for the time-response of the wing's vibration mode shapes rather than the time-response of the wing's individual degrees-of-freedom (assuming the wing can be discretized as a multiple-degree-of-freedom system). In practice, the number of modes needed to represent wing deformation is usually much smaller than the number of physical degrees of freedom, thereby representing a computational savings within the structural domain. The wing's vibration modes can be pre-computed analytically for simple structures or via finite element for more complex structures. The structural model framework originated in Ref. 43 and was extended in Ref. 44, and is summarized here to provide context to the present work. For a more thorough derivation, the reader is encouraged to refer to these references.

Consider a position vector **R** from the wing's fixed point of rotation O to a differential mass element dm located on the wing (Fig. 1). Position vector **R** is

$$\mathbf{R} = \underbrace{x\mathbf{e}_x + y\mathbf{e}_y}_{\mathbf{r}_1} + W(x,y,t)\mathbf{e}_z, \tag{2}$$

where x and y are the planar coordinates of dm (also described by position vector $\mathbf{r}_1$) and $W(x,y,t)$ is a small, unknown out-of-plane elastic deformation dependent on both space and time. The wing's in-plane motion is neglected. The velocity of dm is

$$\dot{\mathbf{R}} = \boldsymbol{\Omega} \times \mathbf{R} + \dot{W}(x,y,t)\mathbf{e}_z. \tag{3}$$

The wing's kinetic energy T is

$$T = \frac{1}{2}\int_m \dot{\mathbf{R}} \cdot \dot{\mathbf{R}}\, dm, \tag{4}$$

where the above represents an integration of the differential kinetic energy of dm over the wing's mass domain. Next, the potential energy U resulting from the wing's elastic deformation is

$$U = \frac{1}{2}\int_V \sigma(W,W)\, dV, \tag{5}$$

where σ is a symmetric, quadratic strain energy density function dependent on wing deformation $W(x,y,t)$ and V is the wing's volume. Next, we represent elastic deformation $W(x,y,t)$ via an eigenfunction expansion such that it can be calculated as space dependent mode shapes $\phi_k(x,y)$ multiplied by their time-dependent modal responses $q_k(t)$, given by

$$W(x,y,t) = \sum_{k=1}^{\infty} \phi_k(x,y) q_k(t). \tag{6}$$

Vibration modes $\phi_k(x,y)$ can be calculated via finite element or in some cases analytically. Mode shapes are normalized with respect to the wing's mass such that they satisfy

$$\int_m \phi_k \phi_r\, dm = \delta_{kr}, \tag{7}$$

$$\int_V \sigma(\phi_k, \phi_r)\, dV = \omega_k^2\, \delta_{kr}, \tag{8}$$

where δ_{kr} is the Kronecker delta function, and ω_k is the kth natural frequency associated with mode shape ϕ_k.

Finally, we expand the kinetic and potential energies in terms of Eq. (6) and apply Lagrange's equation to determine the equation of motion governing modal response q_k as follows:

$$\ddot{q}_k + 2\zeta_k\omega_k\dot{q} + \left[\omega_k^2 - (\Omega_x^2 + \Omega_y^2)\right] q_k = \dot{\boldsymbol{\Omega}} \cdot \mathbf{b_k} - \Omega_z\, \boldsymbol{\Omega} \cdot \mathbf{a}_k + Q_k, \tag{9}$$

where $\mathbf{a_k}$, $\mathbf{b_k}$ are constant vectors related to the position of the inertial force center of the kth vibration mode defined by

$$\mathbf{a}_k = \int_m \phi_k (x\,\mathbf{e}_x + y\,\mathbf{e}_y)\, dm, \tag{10}$$

$$\mathbf{b}_k = \int_m \phi_k (-y\,\mathbf{e}_x + x\,\mathbf{e}_y)\, dm. \tag{11}$$

The first term in the equation of motion is the modal acceleration. The second term is an empirical viscous damping term, where ζ_k is the wing's kth modal damping ratio. The third term is a time-varying stiffness term dependent on the wing's angular velocity. The modal excitation terms to the right-hand side of the equation of motion are the Euler force, the centrifugal force, and the kth non-conservative aerodynamic force Q_k. Non-conservative aerodynamic modal force Q_k can be determined via the principle of virtual work as follows:

$$Q_k = \int_{S_w} dF_z(x,y,t)\phi_k(x,y)\, dS_w, \tag{12}$$

where dF_z is the differential aerodynamic force acting in the z direction and S_w is the wing's surface. The physical aerodynamic force F_z can be determined via any fluid model, including DBET and UVLM.

Finally, we determine the inertial moments $\mathbf{M}_0$ acting at the wing's point of rotation O. The inertial moments are needed to calculate the instantaneous power delivered to the flapping wing. We use a derivation from,[13] which derives $\mathbf{M}_0$ starting from angular momentum $\mathbf{H}_0$. The angular momentum of a rotating, flexible wing is

$$\mathbf{H}_0 = \int_m \mathbf{R} \times \dot{\mathbf{R}}\, dm, \tag{13}$$

which can be expanded via the wing's mode shapes and modal responses as follows:

$$\mathbf{H}_0 = \mathbf{I}_0\boldsymbol{\Omega} + \sum_{k=1}^{\infty}\left[-q_k(\mathbf{a}_k \cdot \boldsymbol{\Omega})\mathbf{e}_z - \mathbf{b}_k\dot{q}_k - (\mathbf{e}_z \cdot \boldsymbol{\Omega})\mathbf{a}_k q_k + (\boldsymbol{\Omega} - \omega_z\mathbf{e}_z)q_k^2\right], \tag{14}$$

with $\mathbf{I}_0$ being the inertial tensor of the wing. The inertial moments about fixed point O can then be determined by differentiating angular momentum $\mathbf{H}_0$ with respect to time, yielding

$$\mathbf{M}_0 = \boldsymbol{\Omega} \times \mathbf{H}_0 + \dot{\mathbf{H}}_{0,xyz}. \tag{15}$$

2. Deformable blade element theory

Blade element theory (BET) is a quasi-static modeling approach that is used frequently to estimate the aerodynamic forces and moments acting on flapping wings.[38,45,46] BET is usually formulated via multiple sets of algebraic equations and is thus computationally efficient. On the other hand, BET has several limitations; it neglects spanwise flows, vortex shedding, wing–wake interactions, and other phenomena that rely on the time history of the surrounding fluid. Further, BET does not provide information about the spatial force distribution acting over the wing. Nonetheless, BET provides order-of-magnitude propulsive force estimates and has been applied extensively to describe the aerodynamics of rigid wings. In the present work, we expand the BET approach to accommodate wing deformation. We refer to this framework as deformable blade element theory (DBET). We neglect added mass and rotational lift terms, which are included in some BET formulations.

A quasi-static differential aerodynamic force dF acting on an airfoil (Fig. 2) is described by

$$dF_{[\cdot]} = \frac{1}{2}\rho_f C_{[\cdot]}(\mathcal{A})\mathbf{V}_\infty \cdot \mathbf{V}_\infty\, dS, \tag{16}$$

where ρ_f is fluid density, $\mathbf{V}_\infty$ is the induced or free stream velocity, $C_{[\cdot]}$ is an aerodynamic coefficient ($[\cdot]$ is a placeholder to indicate either lift or drag) dependent on angle of attack $\mathcal{A}$, and dS is the differential surface over which the differential aerodynamic force acts. Assuming the wing flaps in a quiescent environment, the induced fluid velocity is equal in magnitude and opposite in direction to the wing's velocity, or $\mathbf{V}_\infty = -\dot{\mathbf{R}}$. Then, the differential surface can be described by $dS = c(y)dy$, where $c(y)$ is the wing's chord dependent on location

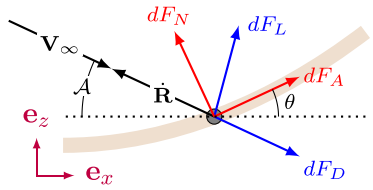

FIG. 2. Free-body diagram showing differential aerodynamic forces acting upon an individual blade element.

along the wing span y and dy is the blade element's width. We assume lift and drag coefficients of the form from[38] as follows:

$$C_P(\mathcal{A}) = C_P \sin(\mathcal{A})\cos(\mathcal{A}), \tag{17}$$

$$C_D(\mathcal{A}) = C_P \sin(\mathcal{A})^2 + C_{D,0}, \tag{18}$$

where C_P and $C_{D,0}$ are empirical aerodynamic coefficients. $C_{D,0}$ represents the drag the wing experiences at zero angle of attack. Since the wing is infinitely thin, this term effectively scales the total shear load acting over the wing's surface. The angle of attack $\mathcal{A}$ is defined as the angle between the wing's velocity vector and the x axis and is calculated via

$$\mathcal{A} = \tan^{-1}\left(\frac{\dot{\mathbf{R}} \cdot \mathbf{e}_z}{\dot{\mathbf{R}} \cdot \mathbf{e}_x}\right). \tag{19}$$

Drag acts collinear to the wing's velocity vector and lift acts orthogonal to drag. Differential lift and drag components dF_L and dF_D must be rotated by $\mathcal{A}$ to determine the differential aerodynamic forces acting normal to the deformed wing dF_N and axial to the deformed wing dF_A. This transformation is given by

$$dF_N = dF_D\cos(\mathcal{A}) + dF_L\sin(\mathcal{A}), \tag{20}$$

$$dF_A = -dF_D\cos(\mathcal{A}) + dF_L\sin(\mathcal{A}). \tag{21}$$

The normal and axial forces do not coincide with the wing's x–z coordinate basis (Fig. 2). To determine the aerodynamic forces acting in the x and z directions, the normal and axial forces must be rotated by the wing's local angle of rotation θ, where θ arises from wing deformation.

3. Quasi three dimensional unsteady vortex lattice method

The unsteady vortex lattice method (UVLM) is an established method, described in detail by Katz and Plotkin.[47] It is a potential flow method governed by

$$\nabla^2\boldsymbol{\Phi} = 0, \tag{22}$$

where $\boldsymbol{\Phi}$ is the velocity potential. As such, the fluid is considered incompressible throughout and irrotational except on the surface of the wing and in the wake. Viscous forces are ignored.

The wing is divided spanwise into multiple blades, each with a constant chord length. The aerodynamic loads on each blade are determined using a 2D UVLM solver. The blade is divided chordwise into panels. Each panel has a bound vortex attached at the quarter-chord and a control point at three-quarters-chord (Fig. 3).

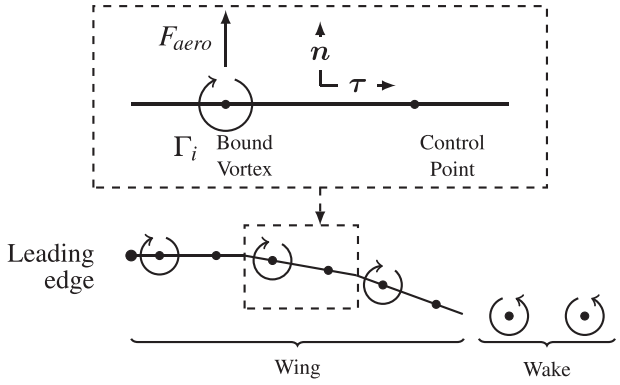

FIG. 3. Panel discretization used by the 2D UVLM solver.

Additionally, the trailing-edge panel sheds free wake vortices which are convected with the flow. Each vortex induces a tangential velocity field around it, described by the Biot–Savart law,

$$\boldsymbol{V}_{\text{ind}} = \frac{\Gamma_j}{2\pi}\frac{(r_{i,z}-r_{j,z})\mathbf{e}_x + (r_{j,x}-r_{i,x})\mathbf{e}_z}{|\boldsymbol{r_i}\text{-}\boldsymbol{r_j}|^2}, \tag{23}$$

where $\boldsymbol{V}_{\text{ind}}$ is the velocity at some point $\boldsymbol{r_i}$ induced by a vortex located at $\boldsymbol{r_j}$, and Γ_j is the vortex strength. This results in a singularity; as r gets smaller, the induced velocity becomes unreasonably large. To remedy this, a cutoff radius r_{co} is defined so that within this radius, the induced velocity decreases linearly as separation decreases, and the induced velocity function becomes

$$\begin{aligned}\boldsymbol{V}_{\text{ind}} &= \frac{\Gamma_j}{2\pi}\frac{(r_{i,z}-r_{j,z})\mathbf{e}_x + (r_{j,x}-r_{i,x})\mathbf{e}_z}{|\boldsymbol{r_i}\text{-}\boldsymbol{r_j}|^2}; \quad |\boldsymbol{r_i}\text{-}\boldsymbol{r_j}| > r_{co},\\ \boldsymbol{V}_{\text{ind}} &= \frac{\Gamma_j}{2\pi}\frac{(r_{i,z}-r_{j,z})\mathbf{e}_x + (r_{j,x}-r_{i,x})\mathbf{e}_z}{r_{co}^2}; \quad |\boldsymbol{r_i}\text{-}\boldsymbol{r_j}| \le r_{co}.\end{aligned} \tag{24}$$

At each time step, the strengths of the bound vortices on the wing as well as the newly shed wake vortex are found by enforcing the non-penetration condition; the wing is a solid barrier through which the fluid is unable to flow. This means the fluid can only move across the surface, and the velocity component normal to the wing surface is zero, stipulated by

$$\boldsymbol{V}\cdot\mathbf{n} = 0, \tag{25}$$

where $\boldsymbol{n}$ is the surface-normal vector on the wing and the flow velocity $\boldsymbol{V}$ is in a wing-fixed frame of reference. When this condition is enforced at the control point of each wing panel, this takes the form

$$\begin{bmatrix} a_{1,1} & a_{1,2} & \cdots & a_{1,N_p} & a_{1,N_p+1} \\ a_{2,1} & a_{2,2} & \cdots & a_{2,N_p} & a_{2,N_p+1} \\ \vdots & \vdots & \ddots & \vdots & \vdots \\ a_{N_p,1} & a_{N_p,2} & \cdots & a_{N_p,N_p} & a_{N_p,N_p+1} \\ 1 & 1 & \cdots & 1 & 1 \end{bmatrix} \begin{Bmatrix} \Gamma_1 \\ \Gamma_2 \\ \vdots \\ \Gamma_{N_p} \\ \Gamma_{W_1} \end{Bmatrix} = \begin{Bmatrix} rhs_1 \\ rhs_2 \\ \vdots \\ rhs_{N_p} \\ rhs* \end{Bmatrix}, \tag{26}$$

where aerodynamic influence coefficient $a_{i,j}$ is the surface-normal velocity induced at the control point of panel i by a unit strength vortex on panel j. rhs_i is the total surface-normal velocity at the ith control point due to all other sources—rigid body kinematics, wing deformation, and wake vortices, and rhs^* is the total bound vorticity on the wing. $\Gamma_{1\ldots N_p}$ is the bound vortex strength of the corresponding panel and Γ_{W_1} is the strength of the newly shed wake vortex, equal to the change in total bound vorticity over the wing from the previous time step. The free wake vortices are massless, and follow the local flow velocity induced by the wing bound vortices and other wake vortices as determined from Eq. (23). The pressure jump at the ith panel is found using the unsteady Bernoulli equation[47]

$$\Delta P_i = -\rho_f\left[(-\dot{\boldsymbol{R}}_{\boldsymbol{i}} + \boldsymbol{V}_{ind,i})\cdot\boldsymbol{\tau}_i\frac{\Gamma_i}{ds} + \frac{\partial}{\partial t}\sum_{j=1}^{i}\Gamma_j\right], \tag{27}$$

where ΔP_i is the pressure jump across the ith panel, $\dot{\boldsymbol{R}}_{\boldsymbol{i}}$ is the velocity of the panel ith in the inertial reference frame arising from the rigid body kinematics and the wing deformation, $\boldsymbol{V}_{ind,i}$ is the velocity induced by the ith bound and wake vortices, $\boldsymbol{\tau}$ is the panel surface-tangent vector, and ds is the panel length. The first term on the right-hand side describes the pressure resulting from quasi-steady aerodynamic forces such as lift and drag. The second term accounts for the pressure due to added mass, where the summation is from the leading edge to the ith panel. The aerodynamic force on each panel acts normal to the surface, and the total force on each blade is obtained by summing the x and z components of the panel forces.

C. High-fidelity computational model

Computational fluid dynamics (CFD) is a common approach to solving the Navier–Stokes equations across a discretized domain. These equations are derived from continuum mechanics and serve to maintain conservation of mass and momentum, and are accepted in the engineering community to encompass most physics pertinent to modeling a fluid domain. Finite element analysis (FEA) is a method for modeling the deformations and stresses throughout structures across a wide range of geometry, material properties, and composite assemblies. To build a two-way coupled model to use as a validation tool for the ROMs, we interface a CFD model using Siemens' Star-CCM+ (v15.04.008) to an FEA model using Dassault Systèmes Abaqus 2019 (6.19-1). Communication between the two commercial packages is handled through SIMULIA Co-simulation Engine (CSE).

For a reduction in computational expense, the CFD model uses a Spalart–Allmaras (SA) closure model in a Reynolds-averaged Navier–Stokes (RANS) scheme. RANS models are used throughout turbulent flow research, and the SA was chosen for its efficiency as a one-equation model as well as its previous use in studying flapping wing aerodynamics.[48,49] This modeling technique was used to calculate the pressure across the wing's surface as influenced by the entire flow field. To resolve this flow field accurately without remeshing the entire fluid domain at each time step, we used a Chimera mesh approach to keep a consistent discretization around the rotating wing.[50] This allows for a finely discretized region surrounding the wing (the *overset* mesh) to move with prescribed kinematics while the surround fluid domain discretization (the *background* mesh) remains motionless (Fig. 4). At each time step, the overset mesh region is cut from the background mesh, and overlapping cells along the edges of the overset region are used to interpolate data between the two meshes,

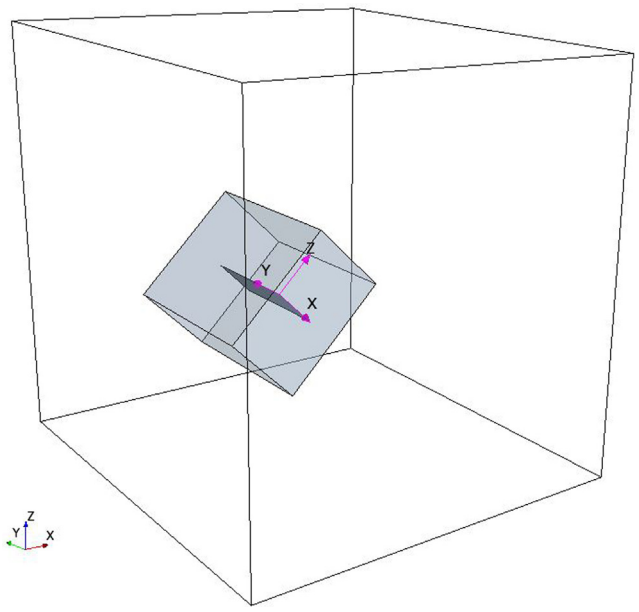

FIG. 4. Background mesh (outlined) and overset mesh (light gray) of the fluid domain in Star-CCM+. The rectangular wing is seen in the dark gray within the overset mesh. The wing-fixed coordinate system is shown in pink, with an origin at the wing root's leading edge. The background mesh must be large enough to accommodate flapping kinematics and encompass pertinant flow features, while the overset mesh must accommodate the out-of-plane deformation of the wing.

thereby maintaining the conservation of mass and momentum. A radial basis function (RBF) mesh morphing algorithm is also applied to the overset mesh, allowing these cells and the overset region boundary to stretch and compress to accommodate the deformation of the wing as calculated in FEA.

The deformations calculated in FEA are influenced by the centrifugal and Euler forces associated with flapping motions as well as the aerodynamic forces calculated by CFD at every time step. We applied the flapping kinematics by imposing angular velocity-dependent boundary conditions at the wing's fixed point of rotation. Abaqus' implicit solver was then used to resolve deformations, which were in turn sent back to CFD.

The communication between FEA and CFD facilitated by SIMULIA CSE allowed us to capture aeroelastic interactions through bilateral coupling, as data are transferred between both software at every time step specified in CFD (Fig. 5). After CFD initializes the motionless fluid domain, kinematics are applied in FEA, and deformations due to inertial and centrifugal forces are resolved. Abaqus uses a dynamic time step to allow for a converged structural solution at each time step, but when the time step specified in CFD has been reached, the new wing geometry is sent to Star-CCM+ CFD in the inertial and wing-fixed frames. This change in geometry is then interpreted as movement of the wing boundary in CFD caused by both the rotation and deformation. Next, the overset mesh region is rotated by the flapping kinematics, and then is morphed based on the wing deformations. Finally, the entire fluid domain in CFD is resolved, and the resulting distribution of aerodynamic forces is sent back to Abaqus FEA. In FEA, the process continues, now adding the aerodynamic forces into the calculation of wing deformation. This cycle continues until a user-specified solution time is reached.

The HiFi model makes minimal assumptions about insignificant physics parameters aside from those associated with the influence of turbulence on the fluid domain as modeled with the SA RANS model. This allows the HiFi model to capture some of the physics that the ROMs ignore, such as spanwise flow which is clearly resolved by the three-dimensional application of the Navier–Stokes equations, and the influence of added mass which is captured through the acceleration term of the conservation of momentum.

III. NUMERICAL SIMULATION PARAMETERS

We now establish the simulation parameters necessary to implement and compare the HiFi model and ROMs. We investigate a thin, homogeneous rectangular wing with flapping kinematics idealized from those of a flying insect. We consider three modulus values (flexible, medium, and stiff hereafter) to explore the influence of flexibility on deflection and aerodynamic forces/moments. The wing is assumed to have a rigid leading edge. All rotations are assumed harmonic.

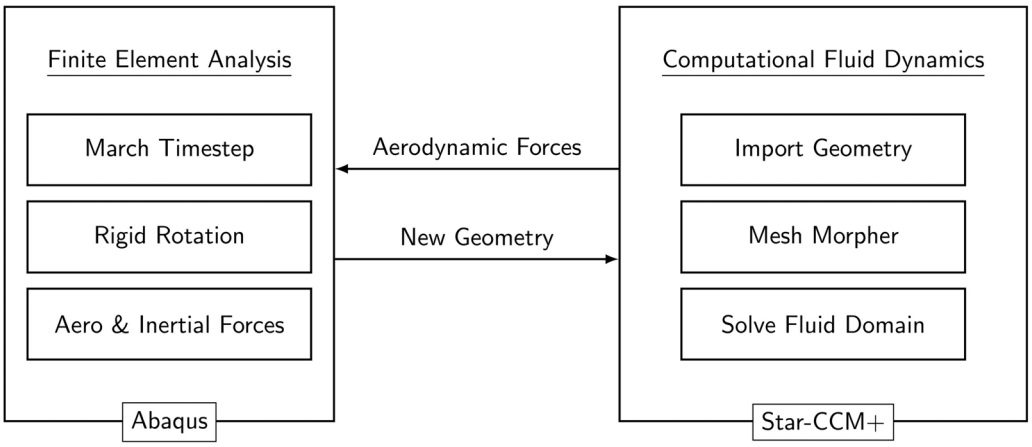

FIG. 5. Bilaterally coupled workflow between Abaqus FEA and Star-CCM+ CFD. This cycle continues at every time step described by CFD.

TABLE I. Wing parameters.

Variable	Description	Value	Unit
L	Wing span	5	cm
c	Wing chord	2	cm
t	Wing thickness	0.17	mm
α_0	Roll amplitude	60	°
β_0	Pitch amplitude	45	°
γ_0	Yaw amplitude	0	°
⋯	Pitch phase	90	°
f	Flap frequency	10	Hz
ρ	Material density	235.5	kg m^{-3}
E	Elastic modulus	(Flexible) 7.3×10^7	Pa
		(Normal) 1.365×10^8	Pa
		(Stiff) 2.4×10^8	Pa
Re	Reynold's number	4400	⋯

The wing flaps about a stationary point in a quiescent environment, which is most representative of hovering flight. Wing parameters are summarized in Table I, and the geometry is shown in Fig. 6. Wing morphology and flapping kinematics are based roughly on the forewing of the monarch butterfly.[51]

The structural model used in DBET and UVLM ROMs [Eq. (9)] is fully defined by flapping kinematics, wing mode shapes ϕ_k, natural frequencies ω_k, damping ratios ζ_k, and the non-conservative load Q_k. We use a numerical modal analysis implemented via Abaqus to calculate ϕ_k and ω_k. The finite element model used for modal analysis is identical to that used for dynamic simulation in the HiFi model, with the primary difference residing in the solution procedure (finite element details are discussed with HiFi model parameters). Practically, we retain two vibration modes (Fig. 6) for the structural solver, which have natural frequencies ($\omega_1 = 40$ Hz, $\omega_2 = 52.2$ Hz) for the flexible wing, ($\omega_1 = 55$ Hz, $\omega_2 = 74.6$ Hz) for the medium wing and ($\omega_1 = 73$ Hz, $\omega_2 = 99$ Hz) for the stiff wing. Damping ratio ζ_k is set to 5% for both vibration modes. The structural model is solved using MATLAB (V2021b) "ode45" at time steps dictated by the DBET and UVLM ROMs.

Simulation parameters for the DBET and UVLM models are summarized in Table II. The DBET model requires empirical aerodynamic coefficients and reference locations for the angle of attack and where aerodynamic forces are assumed to act. We use aerodynamic coefficients in proximity to the values used in Ref. 38. The angle of attack is referenced from the three quarter chord and aerodynamic forces act at the quarter chord. The wing must be broken into ten blade elements for maximum wing deformation and mean force in the $-X$ direction (opposite of gravity, Fig. 1) to converge. The UVLM model requires the wing to be discretized into blades and both the wing and wake must be discretized into bound and shed vortices. The values for panel count, wake count and time step were determined based on convergence studies for a previous 2D model.[52] On each panel, the bound vortex is placed one quarter chord back from the leading edge and the control point is at three quarter chords from the leading edge. The cutoff radius is selected such that results largely match those found without a cutoff, except that large transient spikes should be reduced. Both models are coded in MATLAB (V2021b).

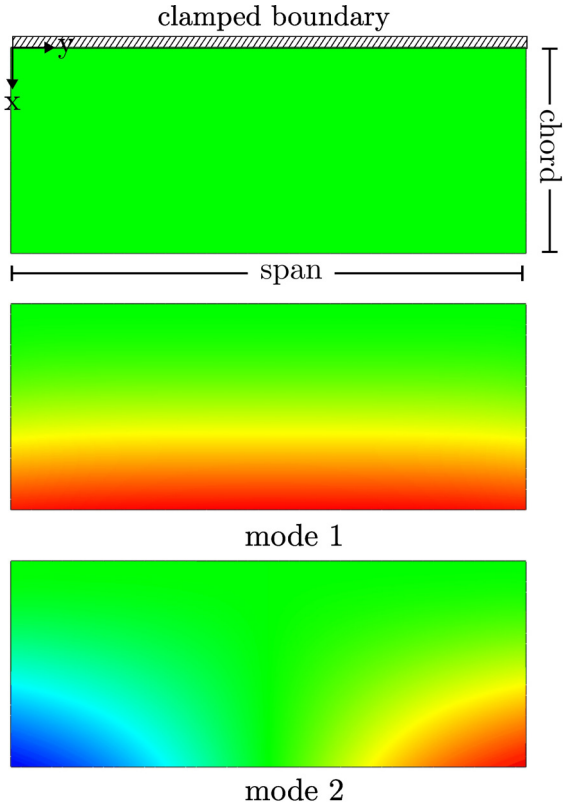

FIG. 6. Geometry and vibration modes of the rectangular wing used in numerical simulation. The first mode represents a chordwise-bending mode, and the second represents a chord-wise torsional mode. Red indicates positive out-of-plane motion, green indicates no motion and black indicates negative out-of-plane motion. Mode shapes are arbitrary in magnitude, which is why a colorbar is omitted.

Parameters for the HiFi model are summarized in Table III. The CFD domain size was chosen with sufficient distance behind the wing's trailing edge and away from the wing's tip to capture flow structures releasing from the wing that could affect the transient fluid forces acting on the wing. The overset mesh size was chosen to capture the

TABLE II. DBET and UVLM simulation parameters.

Variable	Description	Value	Unit
DBET			
C_P	Pressure coefficient	2.9	⋯
$C_{D,0}$	Drag offset coefficient	0.1	⋯
N_s	Number of blades	10	⋯
N_t	Steps-per-wingbeat	100	⋯
UVLM			
N_s	Number of blades	20	⋯
N_p	Number of panels-per-blade	20	⋯
N_w	Number of wake vortices	100	⋯
N_t	Steps-per-wingbeat	200	⋯
r_{co}	Cutoff radius	0.25c	cm

TABLE III. High-fidelity modeling parameters.

Variable	Description	Value	Unit
Computational fluid dynamics			
μ	Dynamic viscosity of air	1.86×10^{-5}	Pa s
ρ	Density of air	1.18	kg m^{-3}
⋯	Domain dimensions	$0.19 \times 0.21 \times 0.2$	m
⋯	Overset dimensions	$0.04 \times 0.08 \times 0.06$	M
⋯	Mean element length (domain)	1.2	mm
⋯	Mean element length (overset)	0.6	mm
⋯	Total number of elements	3 319 937	⋯
⋯	Prism layers	5	⋯
⋯	Prism layer growth rate	1.5	⋯
Δt	Timestep	0.001	s
Finite element analysis			
⋯	Element type	S4R	⋯
α	Raleigh damping factor	(Flexible) 14.472	⋯
		(Normal) 19.858	⋯
		(Stiff) 26.344	⋯
⋯	Number of nodes	1071	⋯
⋯	Shell thickness	0.17	mm
⋯	Number of shell element integration points	5	⋯
Δt_{min}	Minimum automatic timestep	1×10^{-6}	s
Δt_{max}	Maximum automatic timestep	0.001	s

flow structures immediately surrounding the wing with higher resolution and to allow for large wing deformations without over-compression or elongation of any elements by the mesh morpher. An earlier study involving single degree of freedom flapping of a rigid wing with identical geometry revealed converged results with 1.2-mm-sized elements in the domain region and 0.6-mm elements in the overset region.[53] Within the same study, we determined an adequate time step for solution convergence was 0.001 s. At each time step, 25 inner iterations were used to resolve the Navier–Stokes equations, based on convergence of the model residuals. These meshing and time-stepping studies were performed with a rigid wing, so mesh refinement was increased modestly to account for the additional motion of the wing's deflection.

The finite element structural model was comprised of 1000 four-node quadrilateral (S4R) shell elements (1071 nodes), which was sufficient for the wing's first two natural frequencies to converge. We used an automated dynamic time step within FEA, where the minimum time step used was 1×10^{-6} s and the maximum time step was 0.001 s when deformation data were saved and passed to Star-CCM+ CFD. The wing was modeled with a rigid leading edge by applying kinematic constraints to all nodes along this edge to a control point at the wing's point of rotation *O*. At *O*, angular velocity boundary conditions were applied to prescribe the flapping kinematics which the entire leading edge rigidly followed. We use a Rayleigh damping model and select Rayleigh damping factor α such that the first two vibration modes have a damping ratio of 5%, consistent with the ROMs.

IV. RESULTS

Across all models and wing stiffness values considered, we compared wing deformation, aerodynamic forces in the inertial and wing-fixed reference frames, and total moments in the wing reference frame. Wing deformation was compared on the trailing edge at the wing root and wing tip (Fig. 7). In general, the agreement between all models is acceptable. In the most flexible case, the wingtip deflected about 5–5.5 mm, or 25% of the chord length. Maximum deflections predicted by each model are similar, with the ULVM over-predicting the peak value by about 10% compared to the HiFi model. Since both DBET and UVLM ROMs rely on the same structural solver, the difference in response amplitude must stem from differences in fluid loading. The UVLM induces greater deflection, possibly due to an added mass force that is absent from the DBET model. ROM error decreases as the wing becomes stiffer and deformations are reduced. All models indicated that the wing root experienced lower deflections than wing tip (maximally 3.5–4 mm), likely because of increased aerodynamic loading near the wingtip. Aerodynamic loads generally increase along the span (unless in close proximity to the wingtip, where pressure losses occur) due to increasing velocity. The difference in deformation between wingroot and wingtip indicates at least two vibration modes (Fig. 6) are excited during flapping. If deformation was dominated by the first mode, wing deformation would vary only from leading edge to trailing edge and would be nearly uniform from root to tip. At both wingtip and root, deformation occurred at the primary flapping frequency with lower harmonics at three times the flapping frequency superimposed on the response. The primary response from the HiFi model leads that of UVLM, which in turn leads the DBET model. The deformation time lag observed in the ROMs stems from a lag in aerodynamic loading relative to the HiFi model.

To better compare full-field deformation, we generated a contour plot of wing deformation at 1/8 intervals of a single wingbeat. Figure 8

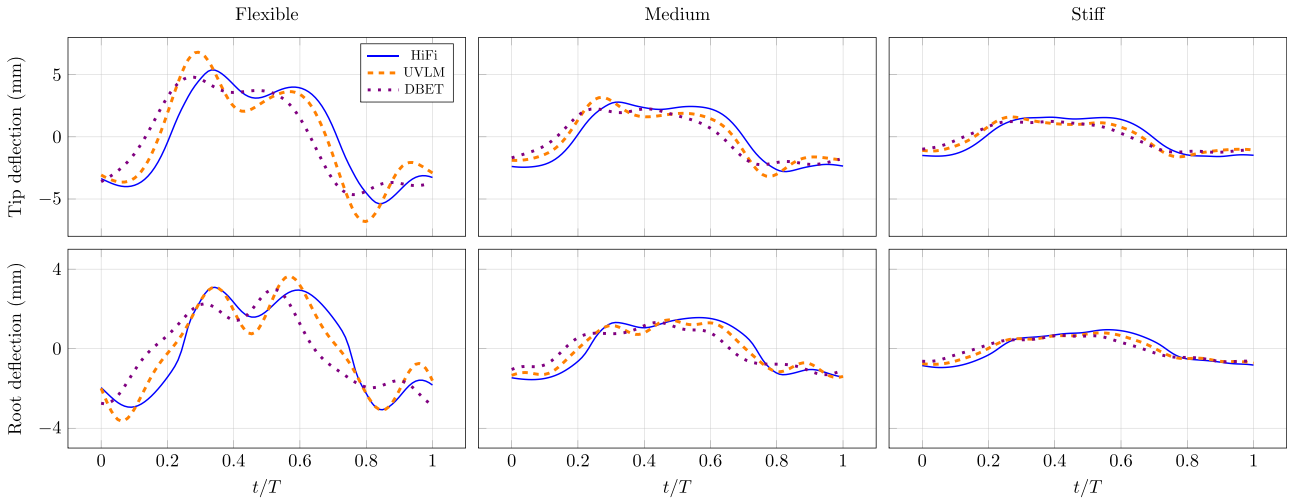

FIG. 7. Deflection of the wing's trailing edge at tip and root locations along the wing's span.

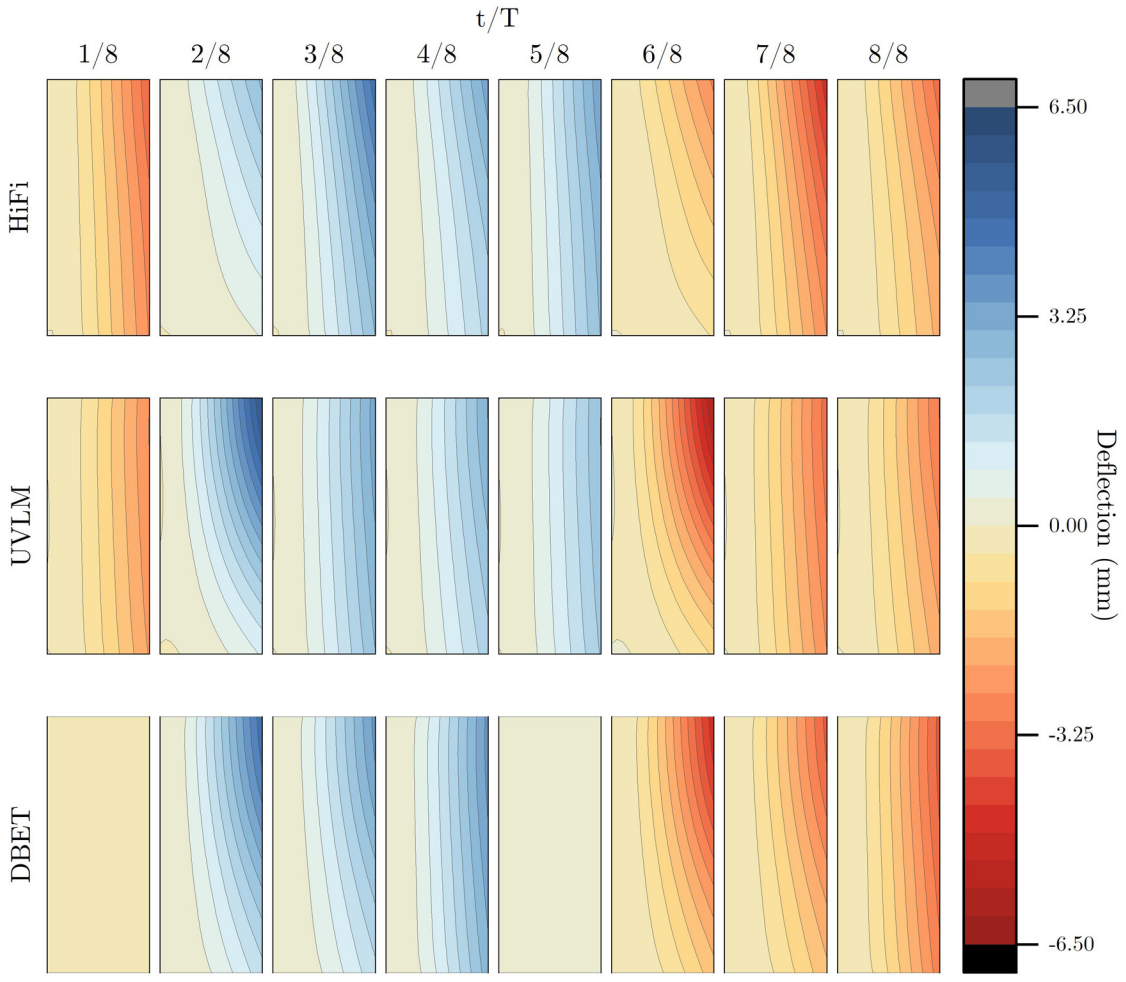

FIG. 8. Contour map showing out-of-plane deformation of the flexible wing as a function of wingbeat period *T*.

shows the out-of-plane deflection predicted by each model for the flexible wing, which is the worst-case scenario in terms of model agreement since the ROMs more closely agree with the HiFi model at smaller deflections (Fig. 7). At most intervals, the deflection contour matches fairly well. Noticeably, DBET indicates near zero deflection at $T/8$ and $5T/8$, whereas the UVLM and HiFI models show non-zero contour profiles. This discrepancy occurs due to the time-lag between DBET and HiFI deflections. Those instances aside, these results suggest that the structural model employed by the ROMs captures deformation profiles reasonably well with only two vibration modes retained, at least for this wing design. As discussed previously, the largest deformation occurs near the wing tip while the root experienced lower deformation by comparison.

Aerodynamic forces with respect to the wing fixed reference frame are shown in Fig. 9. For all wing stiffnesses, the predominate forces act in the wing z direction. For the most flexible case, the absolute peak forces predicted via the HiFi model are about 4, 1, and 0.2 mN in the wing z, x, and y directions, respectively. F_z agrees well across all models. UVLM and CFD produce nearly identical results, while DBET indicates a slight phase lag and lower amplitude in F_z. All models show that F_z increases with wing stiffness, likely because the wing's normal vectors remain more closely aligned with z at lower deflections. The agreement between ROMs and HiFi models is not as strong within the wing-fixed x direction, due in part to differences in how shear is accounted for. The UVLM entirely lacks shear loads, leading to it underestimate F_x compared to CFD and DBET for stiffer wings. The difference is primarily in force amplitude, as the general waveforms agree reasonably well. The agreement is better for more flexible wings, where a larger percentage of F_x stems from pressure loading. DBET produces similar F_x from mid-stroke to stroke reversal ($t/T = 0$ to $t/T = 0.25$) for all wing stiffnesses, but force profile then diverges until next mid-stroke at $t/T = 0.5$. All three models predict a reduction in F_x as the wing is made stiffer, which is opposite to the trend observed in F_z. This is because at larger deflections, the wing's normal vectors have a larger component in the wing's x direction. Due to the lack of spanwise flow, neither DBET nor UVLM are well-positioned to estimate F_y; they are therefore omitted from Fig. 9. Nonetheless, the HiFi model shows the forces in y are considerably lower than the other two force components, and thus we believe it is reasonable to neglect them in ROM efforts.

We next look at total moments at point of rotation O in the wing fixed frame, where the total moments are the inertial moments less the aerodynamic moments (Fig. 10). M_x generally agrees across all three models and at each level of flexibility, though there is a phase discrepancy which may introduce error when calculating quantities from moments such as mechanical power. Moments M_y and M_z also agree well in magnitude across the models, but the phase lag of UVLM and DBET predictions with respect to HiFI predictions is more pronounced. The largest error occurs in M_z of the stiffest wing, which is influenced by the wing's F_x and F_y forces. This error likely occurs because neither DBET and UVLM models are capable of resolving F_y, and the UVLM model does not account for shear, thus leading to poor predictions of F_x for stiff wings (Fig. 9). Nonetheless, because the total moments are in large part driven by inertia, minor discrepancies between aerodynamic moments are not manifested as large discrepancies in the total moments.

We now compare aerodynamic forces with respect to the inertial frame, which is of practical importance because a flapping wing insect must produce sufficient lift to stay aloft during hover. Aerodynamic forces in the inertial frame generally shows close agreement between models (Fig. 11). The HiFi model and ROMs estimate lift forces F_X (recall that gravity is aligned in the $+X$ direction, Fig. 1) that are

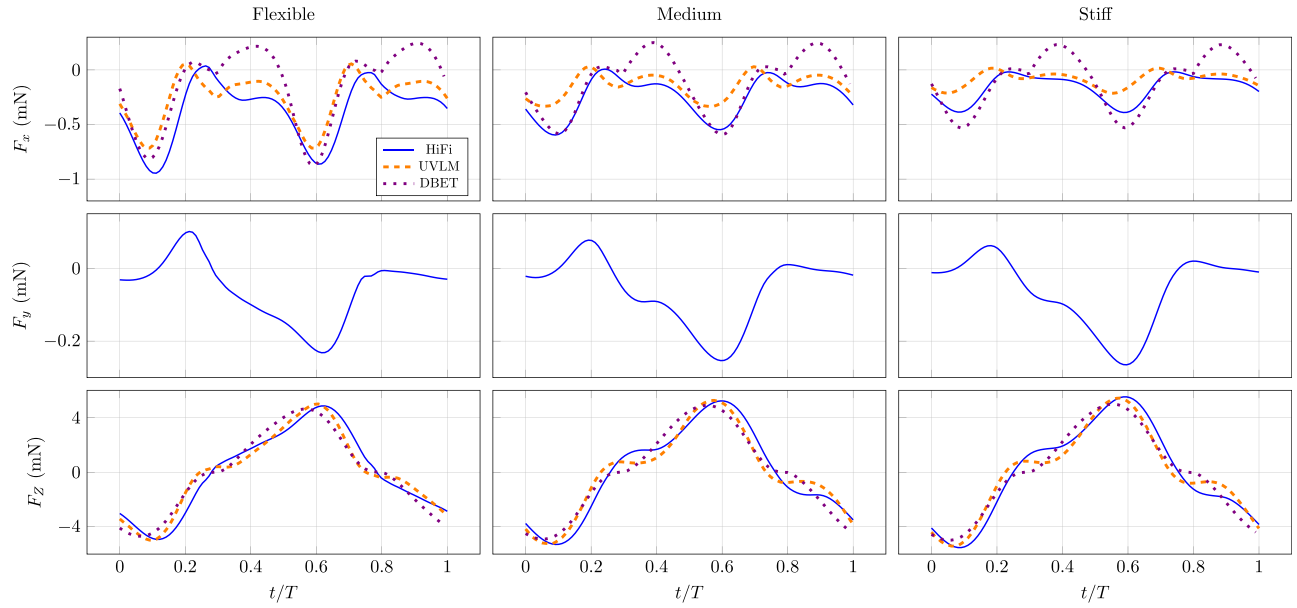

FIG. 9. Aerodynamic forces predicted by each model with respect to the wing-fixed reference frame. UVLM and DBET models do not resolve spanwise flow, so no F_y component is shown for these models.

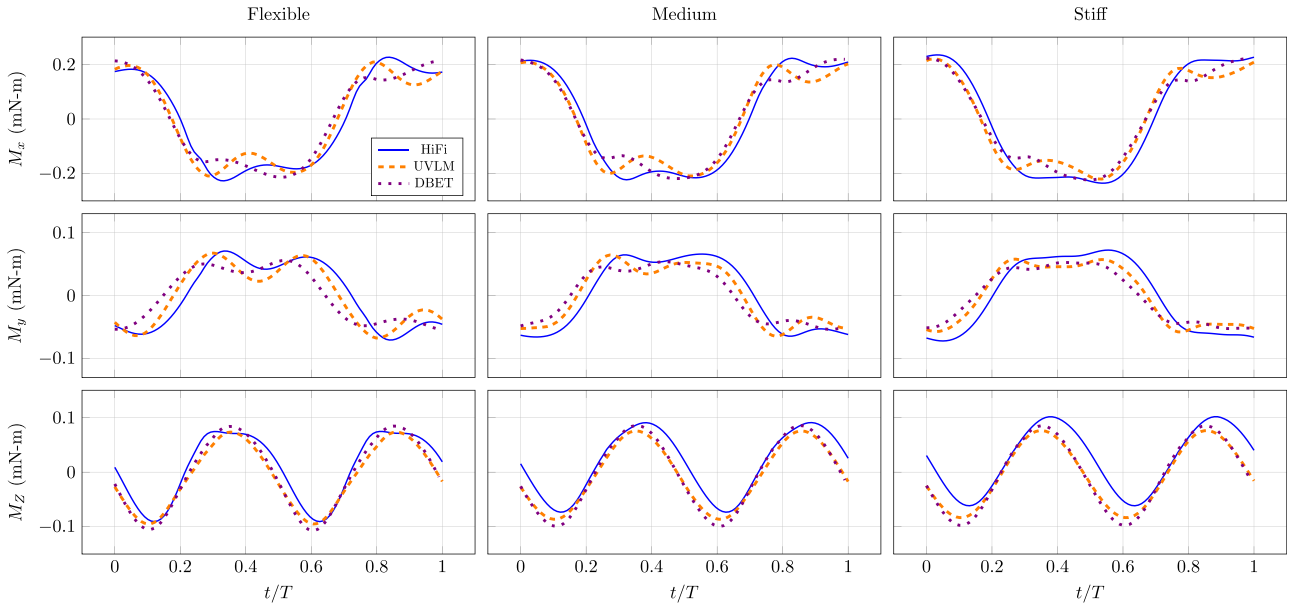

FIG. 10. Aerodynamic moments predicted by each model with respect to the wing-fixed reference frame.

similar in timing and magnitude for each wing stiffness considered. The largest difference in F_X between ROMs and the HiFi model occurs near $t/T = 0.3$, shortly after stroke reversal. This is during the portion of the wing beat when the highest acceleration and wing deflection occur, so this dissimilarity may relate to the differences in how the added mass force is calculated (or in the case of DBET, the lack of added mass). None of the models indicate an increase in lift with wing flexibility; in fact, the more flexible wing produces less lift relative to the stiff wing, though possibly with less input power (see Sec. IV A). The inertial-frame force F_Z is the largest force component in magnitude and agrees well across each model. Similar to wing fixed F_z, world frame F_Z increases with wing stiffness as well. Model agreement is somewhat worse for F_Y, again because neither of the ROMs can accommodate spanwise forces within the wing-fixed frame.

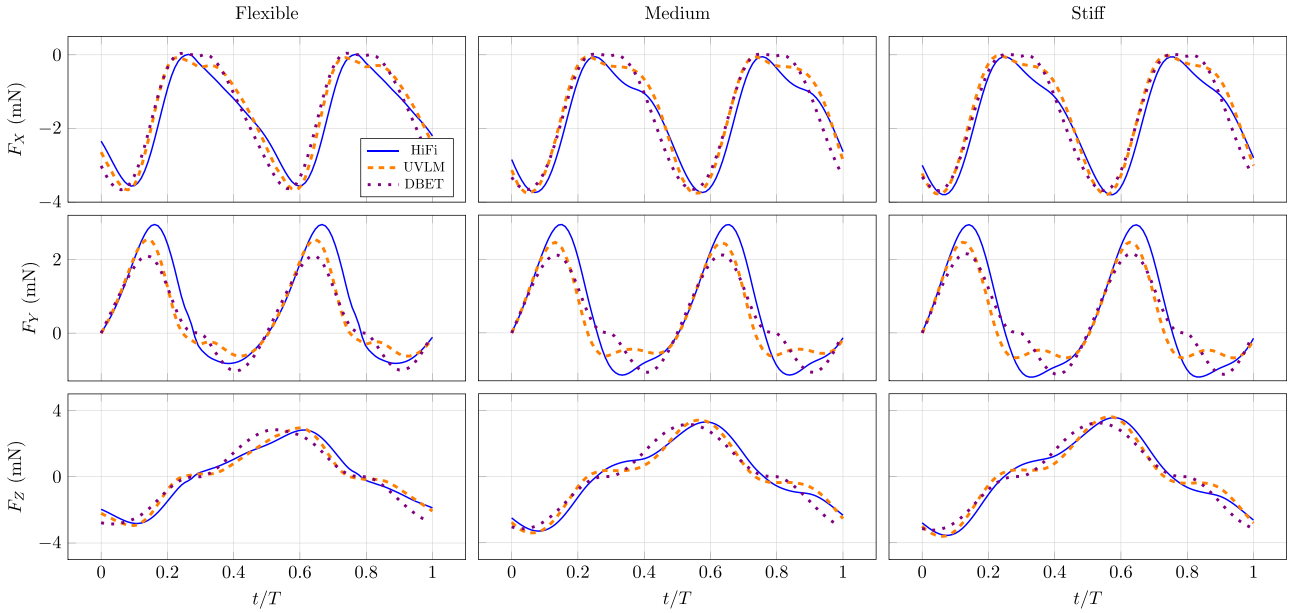

FIG. 11. Aerodynamic forces predicted by each model with respect to the inertial reference frame. Gravity acts in the $+X$ direction.

A. Parametric study

Finally, we perform a parametric study to demonstrate the computational efficiency of the ROMs in exploring wide parameter spaces. We aim to determine how wing stiffness (characterized by the wing's first natural frequency) and mass affect peak deflection, mean lift, and average power at steady state. The average power $\bar{P}$ is calculated via

$$\bar{P} = \frac{1}{T}\int_0^T \mathbf{M}_{total} \cdot \mathbf{\Omega}\, dt, \tag{28}$$

where the total moments are defined by $M_{total} = \mathbf{M}_0 - \mathbf{M}_{aero}$. This expression for power assumes that negative power offsets positive power, or that potential energy is stored in the system and is later recycled to do work. The first natural frequency of the wing was swept from 30 to 100 Hz in 0.1 Hz increments, and we considered discrete wing masses of 40, 60, and 80 mg. Due to the limiting computation time of the high-fidelity model, only the three wing stiffness discussed previously were used in this study. The results are shown in Fig. 12.

As the wing's natural frequency increases, the deflection tends toward zero at a similar rate for all models. The closest agreement was for the 80 mg wing, where the inertial forces dominate the deflection more so than in the lighter wings. In this case, the CFD and DBET line up well at all points, and the UVLM shows only slightly higher wing deformation. As the wing mass increases, the wing deflections predicted by DBET and UVLM diverge, indicating that the differences in the fluid models are responsible for variability in deflection.

The mean lift estimated by CFD is roughly 10% higher than that of the reduced-order models. However, all models show the same general trend, where the wing produces more lift as it becomes more rigid. The lower lift estimated by UVLM may result from the lack of LEV, a feature which is believed to contribute significantly to force production in flapping wings.[54] The lower lift estimated by DBET stems from the aerodynamic coefficient C_P, which may be inflated to increase the lift curve. Wing mass did not have a considerable effect on mean lift.

UVLM and DBET produce nearly the same mean lift $(-F_X)$ from the stiffest case all the way down to moderate levels of flexibility. At higher wing masses, the similarity persists for lower natural frequencies. As the natural frequency is reduced toward 30 Hz (three times the flapping frequency), the DBET and UVLM begin to diverge. However, at this level of compliance, the wing deformation is about 75% of the chord length, and the linear structural framework is likely unsatisfactory. Aerodynamic forces in this range should be interpreted with caution.

The last quantity examined is power consumption. All three methods show that more flexible wings require less power than stiffer wings, and that more massive wings require more power than lighter wings. UVLM and HiFi models show that power steadily decreases with natural frequency. DBET predicts less of a dependence on wing stiffness, though it does still decrease with natural frequency. CFD shows a much steeper relation between stiffness and power than either of the ROMs, perhaps because of shear that is unmodeled by the UVLM model and underestimated by the DBET model. Errors in power are also sensitive to the relative phase between total moments and angular velocity, the latter which is identical across all models. Thus, small errors in total moment phase (Fig. 10) may cause larger

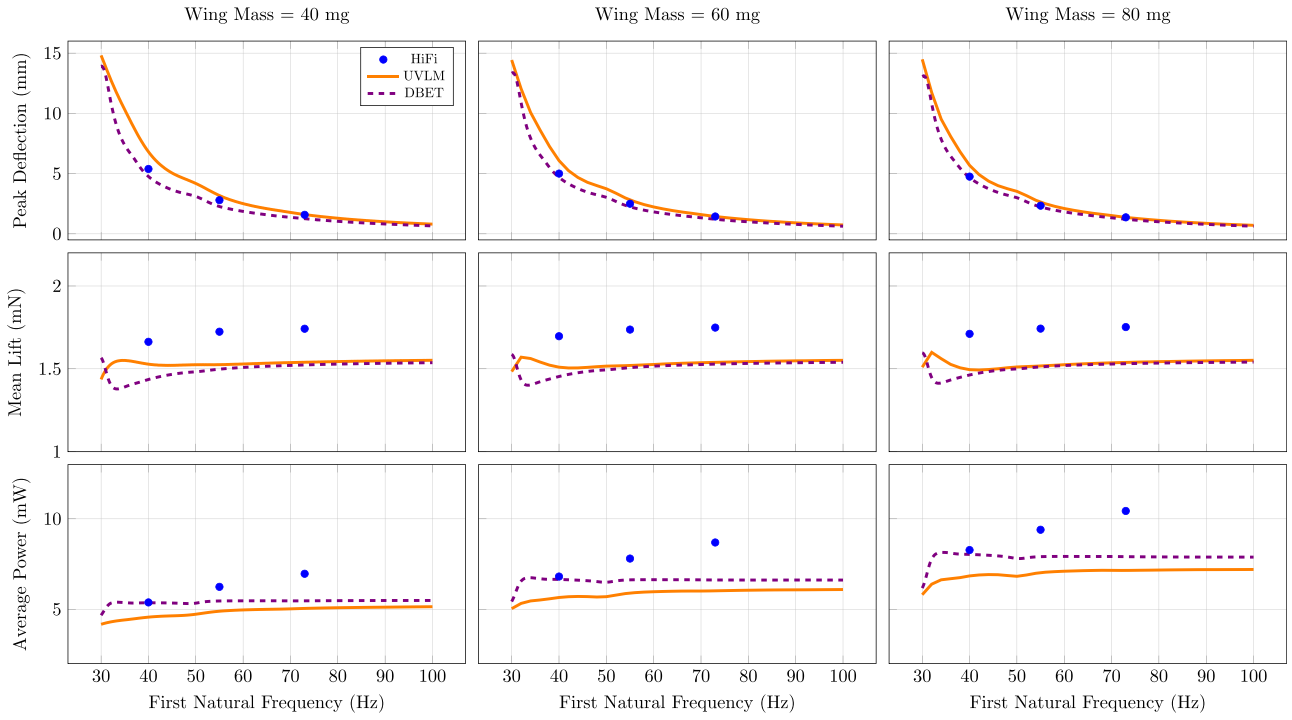

FIG. 12. Parameter study showing the effect of wing flexibility (parametrized by the wing's first natural frequency) and mass on peak deflection, mean lift, and average power. The corresponding time-series data for lift and deflection is shown for the 60 mg wing at natural frequencies of 40, 55, and 73 Hz in Figs. 7 and 11.

errors in power. Still, these studies support the idea that moderate wing flexibility can increase aerodynamic performance, and that the reduction in power consumption outweighs the reduction in lift.

V. DISCUSSION

Wing flexibility and deformation are essential to sensory function and aerodynamic performance in flapping wing insect flight. However, the high-order models used to evaluate flapping wing FSI usually require considerable computational resources, rendering them impractical for parameter studies that consider variable wing stiffness, morphology, or flapping kinematics. In this work, we present two quasi-3D ROMs capable of estimating wing deformation and the resulting aerodynamic forces and moments. Both ROMs rely on a modal truncation-based structural framework but differ in their fluid models. The first ROM uses an algebraic DBET fluid model, and the second ROM uses a UVLM approach. We applied the models to estimate the dynamics of a thin, flexible, rectangular plate with a rigid leading edge subject to rotational kinematics modeled after insect flapping. We compared wing deformation, aerodynamic forces, and total moments predicted by the ROMs to those determined by more conventional HiFi modeling. Both ROMs predicted wing deformation with good accuracy, even when deflections were as large as 25% of the chord length. The ROMs resolved predominate aerodynamic forcing in wing-fixed and inertial reference frames fairly well, but were less accurate in resolving the smaller forces acting in the wing's x–y plane. We then performed a parametric study to demonstrate the influence of wing mass and stiffness on wing deflection, average lift, and average power. The ROMs predicted peak deflection and mean lift fairly well, but had larger discrepancies in average power for stiffer wings. In the following, we discuss the relevance of these ROMs within the study of flapping wing FSI.

A. Computational efficiency

Overall, the computational savings conferred by the two ROMs render them useful tools for studies that require exploration of broad parameter spaces. Direct computational modeling is computationally intensive—within CFD, resolving only the conservation of mass, conservation of momentum, and closure model equations for 25 iterations on each element yields nearly 250×10^6 equations to solve at every time step. Within FEA, the wing is treated as geometrically nonlinear and consequently each time step of analysis must be broken into smaller increments such that a particular solution path may be followed. Considering each node of an S4R element has six degrees-of-freedom, and the plate model has 1071 nodes, about 6×10^3 equations must be solved at each increment within the FEA solver. Thus, computational expense is the biggest motivator for reduced order modeling.

The ROMs were determined to be much faster at modeling bulk propulsive forces and wing deformation relative to the high-fidelity modeling approach. All simulations were performed on a desktop computer custom built for this HiFi setup. We used 10 threads of an intel i9–9900K processor operating with a 4.7 GHz clockspeed, with 64 GB of available DDR4 RAM. When comparing solution times for the flexible wing, the HiFi model resolves the aerodynamic forces and wing deformation in about 5.4 h per wingbeat, the UVLM model about 2.5 s per wingbeat, and the DBET model about 0.093 s per wingbeat. This results in 4 and 6 orders of magnitude in time savings for UVLM and DBET, respectively, demonstrating that ROMs hold value anytime that computational efficiency in needed. We show a practical parameter study where 2100 mass/flexibility combinations were simulated by the ROMs (Fig. 12), taking 7.3 h of computation time for UVLM and 16.3 min for DBET. To gather the same data using the HiFi model would have taken approximately 6.5 years.

B. Applications of ROMs

ROMs play an important role in the study of insect flight. Across species, insect wings have distinct morphological features and flapping kinematics that influence wing strain profiles, sensing and aerodynamic performance. The effect of morphology and flapping kinematics is difficult to fully address using HiFi models. Though ROMs have lower accuracy relative to direct computational approaches, they allow parameter spaces to be explored more effectively. HiFi modeling can then be used for a subset of conditions to ensure ROM accuracy.

Both of the ROMs presented in this work are general in the sense that they can accommodate arbitrary wing geometry, morphology and flapping kinematics. As discussed in Sec. II B 1, the reduced-order structural model is versatile because it can interface with modal-based finite element solvers. The ability to pre-compute mode shapes in FEA allows the user significant freedom and creativity in the geometry and structural domain to investigate the effects of a wide range of biological or engineering-inspired wing designs. Further, physical experimentation like scanning laser vibrometry could be used to compute mode shapes of biological wings,[40] allowing for deeper study of real insect wings. Any number of mode shapes can be included in the models when deemed appropriate. Practically, the number of modes retained generally corresponds to the modes with natural frequencies that fall within ten times that of the predominant excitation frequency.

C. ROM limitations

Despite the advantage of the flapping wing FSI ROMs, each has limitations that constrain their accuracy in some contexts. First, both the quasi-3D DBET and UVLM ROMs neglect spanwise flow. Spanwise flow is a critical for modeling effects like shed vortices from the wingtip that result in downwash and induced drag.[55] Without spanwise flow, it is not possible for fluid to wrap around the wingtip in any way. Quasi-3D approaches will consequently overestimate the fluid loading near the wingtip of a structure, which may in turn amplify the deformation of modes with large displacements near the wingtip. If the rigid leading edge assumption employed in this work were relaxed, this modeling error may result in a larger discrepancy between deformations estimated via ROMs and HiFi methods.

Second, both ROMs have limited capacity to describe chordwise pressure distributions. The DBET model provides no force distribution information and instead assumes all aerodynamic forces simply act at the quarter chord. The UVLM model provides some information regarding chordwise pressure variation, but has limited accuracy near the leading edge because the LEV is not explicitly modeled. The LEV is considered a major factor in lift generation.[54] The UVLM method assumes that flow is always attached to the wing until wake vortices are shed from the trailing edge. This means that wing motions at angles of attack that would normally induce stall without the LEV are modeled such that flow remains attached over the leading edge, thereby requiring particularly strong V_{ind} used in pressure calculations.

Consequently, we believe the LEV must be considered to improve chordwise pressure estimates.

Third, both ROMs provide limited or no information regarding the flow field surrounding the wing. The DBET model provides only bulk propulsive forces and moments. UVLM cannot resolve the entire fluid domain and, instead, is only tracking some flow features that are shed from the wing. These features are monitored for a user specified amount of time, which could be a cause of error in instances where flow features have a delayed interaction with the wing. This is potentially problematic when fluid flow causes a more spatially varying distribution of aerodynamic force.

These modeling limitations help define the scope and appropriate use these quasi-3D ROMs. While studies sensitive to changes in spanwise flow or spatial distribution of forces should perhaps be left to other methods, studies involving bulk aerodynamics and high computational efficiency benefit significantly. The 4 and 6 orders of magnitude time savings is a clear demonstration of why these models can be advantageous over conventional high-fidelity approaches in parameter studies.

ACKNOWLEDGMENTS

This research was supported the National Science Foundation under Award No. CBET-1855383 to M.J. Any opinions, findings, and conclusions or recommendations expressed in this material are those of the author(s) and do not necessarily reflect the views of the National Science Foundation.

AUTHOR DECLARATIONS

Conflict of Interest

The authors have no conflicts to disclose.

Author Contributions

R. Schwab and J. Reade contributed equally to this work.

Ryan Schwab: Formal analysis (equal); Investigation (equal); Methodology (equal); Software (equal); Validation (equal); Writing – original draft (equal); Writing – review & editing (equal). **Joseph Reade:** Formal analysis (equal); Investigation (equal); Methodology (equal); Software (equal); Validation (equal); Visualization (equal); Writing – original draft (equal); Writing – review & editing (equal). **Mark Jankauski:** Conceptualization (lead); Formal analysis (supporting); Funding acquisition (equal); Methodology (equal); Project administration (equal); Software (equal); Validation (equal); Visualization (equal); Writing – original draft (equal); Writing – review & editing (equal).

DATA AVAILABILITY

The data that support the findings of this study are available from the corresponding author upon reasonable request.

REFERENCES

[1]S. J. Huston and V. Jayaraman, "Studying sensorimotor integration in insects," Curr. Opin. Neurobiol. **21**, 527–534 (2011).
[2]B. H. Dickerson, J. L. Fox, and S. Sponberg, "Functional diversity from generic encoding in insect campaniform sensilla," Curr. Opin. Physiol. **19**, 194–203 (2021).
[3]W. Gnatzy, U. Grunert, and M. Bender, "Campaniform sensilla of *Calliphora vicina* (Insecta, Diptera)," Zoomorphology **106**, 312–319 (1987).
[4]S. P. Sane, A. Dieudonné, M. A. Willis, and T. L. Daniel, "Antennal mechanosensors mediate flight control in moths," Science **315**, 863–866 (2007).
[5]B. R. Aiello, K. E. Stanchak, A. I. Weber, T. Deora, S. Sponberg, and B. W. Brunton, "Spatial distribution of campaniform sensilla mechanosensors on wings: Form, function, and phylogeny," Curr. Opin. Insect Sci. **48**, 8–17 (2021).
[6]B. Pratt, T. Deora, T. Mohren, and T. Daniel, "Neural evidence supports a dual sensory-motor role for insect wings," Proc. R. Soc. B **284**, 20170969 (2017).
[7]B. H. Dickerson, Z. N. Aldworth, and T. L. Daniel, "Control of moth flight posture is mediated by wing mechanosensory feedback," J. Exp. Biol. **217**, 2301–2308 (2014).
[8]A. Eberle, B. Dickerson, P. Reinhall, and T. Daniel, "A new twist on gyroscopic sensing: Body rotations lead to torsion in flapping, flexing insect wings," J. R. Soc. Interface **12**, 20141088 (2015).
[9]B. T. Hinson and K. A. Morgansen, "Gyroscopic sensing in the wings of the hawkmoth *Manduca sexta*: The role of sensor location and directional sensitivity," Bioinspiration Biomimetics **10**, 056013 (2015).
[10]R. J. Wootton, "Support and deformability in insect wings," J. Zool. **193**, 447–468 (1981).
[11]T. Nakata and H. Liu, "A fluid–structure interaction model of insect flight with flexible wings," J. Comput. Phys. **231**, 1822–1847 (2012).
[12]S. A. Combes and T. L. Daniel, "Into thin air: Contributions of aerodynamic and inertial-elastic forces to wing bending in the hawkmoth *Manduca sexta*," J. Exp. Biol. **206**, 2999–3006 (2003).
[13]H. E. Reid, R. K. Schwab, M. Maxcer, R. K. D. Peterson, E. L. Johnson, and M. Jankauski, "Wing flexibility reduces the energetic requirements of insect flight," Bioinspiration Biomimetics **14**, 056007 (2019).
[14]S. Heathcote, Z. Wang, and I. Gursul, "Effect of spanwise flexibility on flapping wing propulsion," J. Fluids Struct. **24**, 183–199 (2008).
[15]M. Moore, "Analytical results on the role of flexibility in flapping propulsion," J. Fluid Mech. **757**, 599–612 (2014).
[16]N. Lee, S. Lee, H. Cho, and S. Shin, "Effect of flexibility on flapping wing characteristics in hover and forward flight," Comput. Fluids **173**, 111–117 (2018).
[17]B. Yin and H. Luo, "Effect of wing inertia on hovering performance of flexible flapping wings," Phys. Fluids **22**, 111902 (2010).
[18]M. Percin, Y. Hu, B. W. van Oudheusden, B. Remes, and F. Scarano, "Wing flexibility effects in clap-and-fling," Int. J. Micro Air Vehicles **3**, 217–227 (2011).
[19]F.-B. Tian, H. Dai, H. Luo, J. F. Doyle, and B. Rousseau, "Fluid–structure interaction involving large deformations: 3D simulations and applications to biological systems," J. Comput. Phys. **258**, 451–469 (2014).
[20]D. Ishihara, T. Horie, and M. Denda, "A two-dimensional computational study on the fluid–structure interaction cause of wing pitch changes in dipteran flapping flight," J. Exp. Biol. **212**, 1–21 (2009).
[21]M. Hamamoto, Y. Ohta, K. Hara, and T. Hisada, "Application of fluid–structure interaction analysis to flapping flight of insects with deformable wings," Adv. Rob. **21**, 1–21 (2007).
[22]T. Fitzgerald, M. Valdez, M. Vanella, E. Balaras, and B. Balachandran, "Flexible flapping systems: Computational investigations into fluid-structure interactions," Aeronaut. J. **115**, 593–604 (2011).
[23]J. Tang, S. Chimakurthi, R. Palacios, C. Cesnik, and W. Shyy, "Computational fluid-structure interaction of a deformable flapping wing for micro air vehicle applications," in *46th AIAA Aerospace Sciences Meeting and Exhibit* (AIAA, 2008), p. 615.
[24]T. Yamada and S. Yoshimura, "Line search partitioned approach for fluid-structure interaction analysis of flapping wing," Comput. Model. Eng. Sci. **24**, 51 (2008).
[25]D. Willis, E. Israeli, P.-O. Persson, M. Drela, J. Peraire, S. Swartz, and K. Breuer, "A computational framework for fluid structure interaction in biologically inspired flapping flight," in *25th AIAA Applied Aerodynamics Conference* (AIAA, 2007), p. 3803.
[26]B. A. Roccia, S. Preidikman, and B. Balachandran, "Computational dynamics of flapping wings in hover flight: A co-simulation strategy," AIAA J. **55**, 1806–1822 (2017).

[27]J. A. John D., *Computational Fluid Dynamics: The Basics with Applications* (McGraw-Hill Education, 1995).
[28]H. Liu, C. P. Ellington, K. Kawachi, C. van den Berg, and A. P. Willmott, "A computational fluid dynamic study of hawkmoth hovering," J. Exp. Biol. **201**, 461–477 (1998).
[29]S. A. Combes and T. L. Daniel, "Flexural stiffness in insect wings I. Scaling and the influence of wing venation," J. Exp. Biol. **206**, 2979–2987 (2003).
[30]M. Smith, P. Wilkin, and M. Williams, "The advantages of an unsteady panel method in modelling the aerodynamic forces on rigid flapping wings," J. Exp. Biol. **199**(5), 1073–1083 (1996).
[31]M. S. Vest and J. Katz, "Unsteady aerodynamic model of flapping wings," AIAA J. **34**, 1435–1440 (1996).
[32]L. N. Long and T. E. Fritz, "Object-oriented unsteady vortex lattice method for flapping flight," J. Aircr. **41**, 1275–1290 (2004).
[33]M. F. Valdez, B. Balachandran, and S. Preidikman, "Comparative study on analytical and computational aerodynamic models for flapping wings MAVs," Aeronaut. J. **124**, 1636–1665 (2020).
[34]B. A. Roccia, S. Preidikman, J. C. Massa, and D. T. Mook, "Modified unsteady vortex-lattice method to study flapping wings in hover flight," AIAA J. **51**, 2628–2642 (2013).
[35]R. K. Schwab, H. E. Reid, and M. Jankauski, "Reduced-order modeling and experimental studies of bilaterally coupled fluid–structure interaction in single-degree-of-freedom flapping wings," J. Vib. Acoust. **142**, 021012 (2020).
[36]Q. Wang, J. Goosen, and F. van Keulen, "An efficient fluid–structure interaction model for optimizing twistable flapping wings," J. Fluids Struct. **73**, 82–99 (2017).
[37]S. Combes and T. Daniel, "Flexural stiffness in insect wings II. Spatial distribution and dynamic wing bending," J. Exp. Biol. **206**, 2989–2997 (2003).
[38]S. M. Walker and G. K. Taylor, "A semi-empirical model of the aerodynamics of manoeuvring insect flight," J. R. Soc. Interface **18**, 20210103 (2021).
[39]C. Fernandez-Escudero, M. Gagnon, E. Laurendeau, S. Prothin, G. Michon, and A. Ross, "Comparison of low, medium and high fidelity numerical methods for unsteady aerodynamics and nonlinear aeroelasticity," J. Fluids Struct. **91**, 102744 (2019).
[40]H. Reid, H. Zhou, M. Maxcer, R. K. Peterson, J. Deng, and M. Jankauski, "Toward the design of dynamically similar artificial insect wings," Int. J. Micro Air Veh. **13**, 1 (2021).
[41]A. G. Norris, A. N. Palazotto, and R. G. Cobb, "Experimental structural dynamic characterization of the hawkmoth (*Manduca sexta*) forewing," Int. J. Micro Air Veh. **5**, 39–54 (2013).
[42]M. Jankauski, T. L. Daniel, and I. Shen, "Asymmetries in wing inertial and aerodynamic torques contribute to steering in flying insects," Bioinspiration Biomimetics **12**, 046001 (2017).
[43]M. Jankauski and I. Shen, "Dynamic modeling of an insect wing subject to three-dimensional rotation," Int. J. Micro Air Veh. **6**, 231–251 (2014).
[44]R. Schwab, E. Johnson, and M. Jankauski, "A novel fluid–structure interaction framework for flapping, flexible wings," J. Vib. Acoust. **141**, 061002 (2019).
[45]G. J. Berman and Z. J. Wang, "Energy-minimizing kinematics in hovering insect flight," J. Fluid Mech. **582**, 153–168 (2007).
[46]S. P. Sane and M. H. Dickinson, "The aerodynamic effects of wing rotation and a revised quasi-steady model of flapping flight," J. Exp. Biol. **205**, 1087–1096 (2002).
[47]J. Katz and A. Plotkin, *Low-Speed Aerodynamics* (Cambridge university Press, 2001), Vol. 13.
[48]W. Geissler and B. G. van der Wall, "Dynamic stall control on flapping wing airfoils," Aerosp. Sci. Technol. **62**, 1–10 (2017).
[49]M. Jones and N. Yamaleev, "The effect of a gust on the flapping wing performance," in 50th AIAA Aerospace Sciences Meeting Including the New Horizons Forum and Aerospace Exposition, 2012.
[50]H. Hadzic, "Development and application of finite volume method for the computation of flows around moving bodies on unstructured, overlapping grids," Ph.D. thesis (Technische Universität Hamburg, Hamburg, 2006).
[51]A. T. Bode-Oke and H. Dong, "The reverse flight of a monarch butterfly (*Danaus plexippus*) is characterized by a weight-supporting upstroke and postural changes," J. R. Soc. Interface **17**, 20200268 (2020).
[52]J. Reade and M. Jankauski, "Investigation of chordwise functionally graded flexural rigidity in flapping wings using a two-dimensional pitch-plunge model," Bioinspiration Biomimetics **17**, 066007 (2022).
[53]R. Schwab, E. Johnson, and M. Jankauski, "Reduced-order modeling and the physics governing flapping wing fluid-structure interaction," bioRxiv (2021).
[54]W. Shyy, H. Aono, S. Chimakurthi, P. Trizila, C.-K. Kang, C. Cesnik, and H. Liu, "Recent progress in flapping wing aerodynamics and aeroelasticity," Prog. Aerosp. Sci. **46**, 284–327 (2010).
[55]J. D. Anderson, *Fundamentals of Aerodynamics*, 5th ed. (McGraw-Hill, 2011).